

DPNet: Doppler LiDAR Motion Planning for Highly-Dynamic Environments

Wei Zuo¹, Zeyi Ren¹, Chengyang Li¹, Yikun Wang¹, Mingle Zhao²,
Shuai Wang^{3,†}, Wei Sui⁴, Fei Gao⁵, Yik-Chung Wu^{1,†}, and Chengzhong Xu²

Abstract—Existing motion planning methods often struggle with rapid-motion obstacles due to an insufficient understanding of environmental changes. To address this limitation, we propose integrating motion planners with Doppler LiDARs which provide not only ranging measurements but also instantaneous point velocities. However, this integration is nontrivial due to the dual requirements of high accuracy and high frequency. To this end, we introduce Doppler Planning Network (DPNet), which tracks and reacts to rapid obstacles using Doppler model-based learning. Particularly, we first propose a Doppler Kalman neural network (D-KalmanNet) to track the future states of obstacles under partially observable Gaussian state space model. We then leverage the estimated motions to construct a Doppler-tuned model predictive control (DT-MPC) framework for ego-motion planning, enabling runtime auto-tuning of the controller parameters. These two model-based learners allow DPNet to maintain lightweight while learning fast environmental changes using minimum data, and achieve both high frequency and high accuracy in tracking and planning. Experiments on both high-fidelity simulator and real-world datasets demonstrate the superiority of DPNet over extensive benchmark schemes. Project page: <https://github.com/UUwei-zuo/DPNet.git>

Index Terms—Model-based learning, motion planning

I. INTRODUCTION

REAL-TIME robot motion planning in highly-dynamic environments is crucial for a broad range of applications, including emergency rescue and autonomous driving [1]. Such scenarios require accurate knowledge of environmental dynamics, which can be leveraged by the motion controller to generate sequences of collision-free actions under kinematic constraints. Existing motion planning methods heavily rely on light detection and ranging (LiDAR) sensors to capture the current positions of the obstacles from the point cloud [2], and then predict obstacles' future trajectories via learning-based [3], physics-based [4], or physics-informed learning [5], [6] methods. But these approaches struggle in handling rapid-motion obstacles due to their limited ability to understand fast environmental changes in real time.

Recently, however, the situation has changed thanks to the remarkable milestone of the emerging Doppler LiDAR sensors, which not only offer the high-resolution point range data but also the point Doppler velocity [7]. The new dimension of Doppler velocity explicitly provides the instantaneous motion information of obstacles, opening up new opportunities for agile motion planning in rapid-changing scenarios. Yet, how to integrate Doppler LiDAR sensors into motion planners

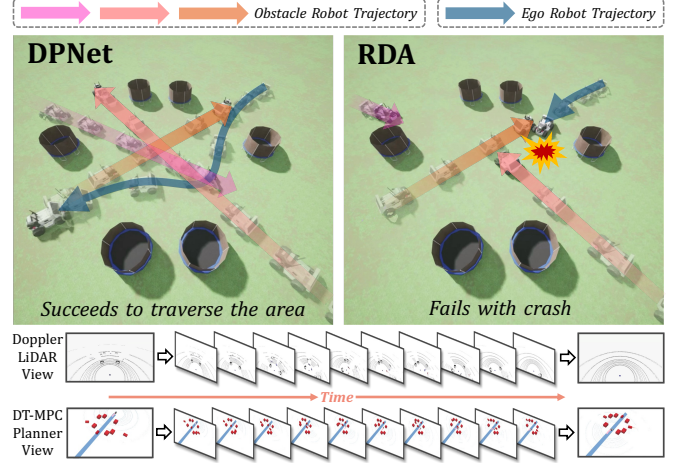


Fig. 1: Doppler model-based learning enables DPNet to understand and traverse highly-dynamic environments.

for a unified solution framework is still unknown. This is nontrivial since the solution should be high-performance, real-time, safety-assured, and work properly with limited onboard computational resources.

Given a certain estimate of the obstacle state, the next step is to conduct motion control. Conventional motion controllers, e.g., model predictive control (MPC), use the estimated dynamics to construct consecutive problems along the horizon [8]. However, they might not work if the prior knowledge about the cost function or the dynamical model is imperfect. To address this problem, emerging auto-tuning motion controllers enable parameter learning from closed-loop execution data [9]. Nonetheless, when applied to dynamic collision avoidance, these tune-from-testing methods typically require an actual collision event to trigger parameter update. To broaden their applications, how to realize run-time controller tuning without relying on actual collisions becomes an important issue.

To fill these research gaps, this paper proposes Doppler planning network (DPNet) shown in Fig. 1, which leverages the new dimension provided by Doppler LiDAR and two key algorithm innovations to achieve environmental motion learning and runtime controller tuning. The first innovation is a Doppler Kalman neural network (D-KalmanNet) which achieves real-time obstacle future state tracking under partially observable Gaussian state space (GSS) model. The D-KalmanNet incorporates the structural GSS model with a recurrent neural network (RNN) and sequences of Doppler velocity measurements, ensuring very high tracking frequency with an ultra-lightweight model size. The second innovation is a Doppler-tuned model predictive control (DT-MPC) framework design, which first performs Doppler-inferred collision check along the future horizon and then tunes the

¹The University of Hong Kong, Hong Kong

²University of Macau, Macau

³Shenzhen Institutes of Advanced Technology, Chinese Academy of Sciences, Shenzhen, China

⁴D-Robotics, Beijing, China

⁵Zhejiang University, Hangzhou, China

[†] Corresponding authors: Shuai Wang (s.wang@siat.ac.cn) and Yik-Chung Wu (ycwu@eee.hku.hk).

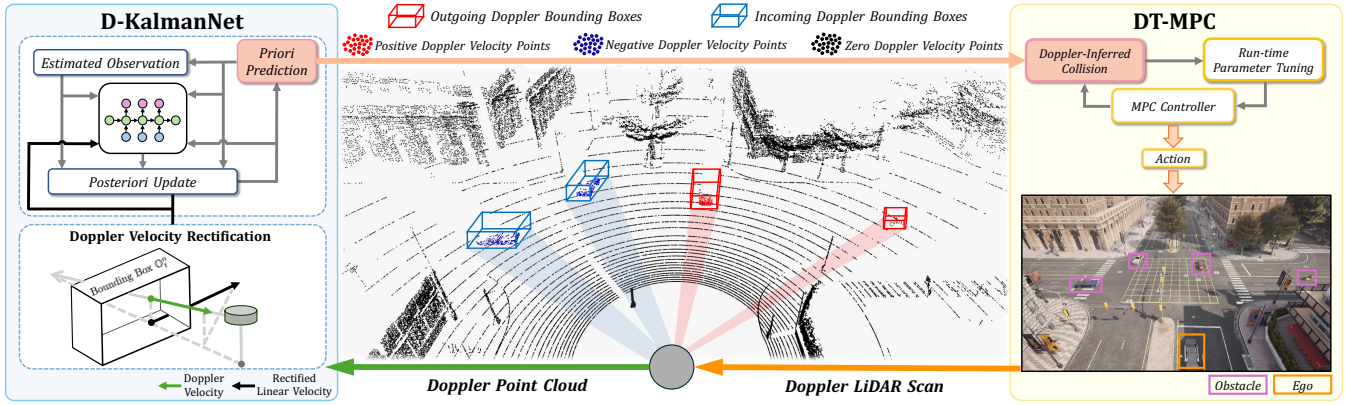


Fig. 2: The proposed DPNet system, which consists of D-KalmanNet and DT-MPC modules.

controller parameters using the imagined collision cost. Under the Doppler guidance, the controller learning can be performed in an online fashion before actual collisions. To reduce the computational cost, a factorization-based method is designed to update controller parameters efficiently and an alternating direction method of multipliers (ADMM) algorithm is used to execute the controller. Built upon the above two innovations, DPNet is able to understand and cope with fast environmental changes using minimum data.

To evaluate DPNet with D-KalmanNet and DT-MPC algorithms, extensive robot operation system (ROS) experiments are performed. We show that DPNet outperforms state-of-the-art planners including RDA [10], MPC-D-CBF [11], and OBICA [12] on diverse metrics in Carla simulator [13]. Ablation studies confirm DT-MPC’s superiority over existing auto-tuning MPC, especially in highly-cluttered environments. Moreover, evaluations on real-world Doppler LiDAR dataset Aevascene [14] demonstrate that D-KalmanNet achieves lowest tracking errors over existing tracking methods including Kalman filter [15] and KalmanNet [5] across wide execution frequency range (i.e., 1–10 Hz), different horizon lengths (1–10), and various road scenarios (i.e., *Highway* and *City*). It is also found that D-KalmanNet can be executed at 15–100 Hz on a low-cost Orin NX 16 GB chip when tracking up to 10 objects simultaneously. To the best of our knowledge, this is the first attempt to integrate Doppler LiDAR with motion planning. Our contributions are summarized as follows:

- We introduce the Doppler LiDAR to support motion planning designs, resulting in a novel DPNet framework. By incorporating the new dimension of Doppler velocity for model-based learning, DPNet can proactively avoid highly-dynamic obstacles.
- We propose D-KalmanNet for obstacle tracking, achieving higher accuracy than existing physical, learning, or hybrid methods, while simultaneously maintaining ultra-low computation cost and high frequency.
- We propose DT-MPC to achieve run-time controller tuning by leveraging Doppler-inferred collision instead of learning from actual collisions.
- We implement the complete DPNet framework, including both D-KalmanNet and DT-MPC algorithms. Extensive results show significant improvements over existing schemes in terms of diverse metrics.

II. RELATED WORK

Doppler LiDAR. In contrast to traditional LiDAR [2], Doppler LiDAR reshapes the landscape of robotic solutions by providing Doppler velocity measurements. It has been used in object detection, state estimation, and simultaneous localization and mapping [16]–[22]. In terms of evaluation, Carla [13] provides realistic Doppler LiDAR simulations [7], [23], and AevaScenes [14] dataset provides on-road Doppler LiDAR recordings. However, all existing research focuses on open-loop perception usages, and integrating Doppler LiDAR into closed-loop motion planning remains unexplored.

Obstacle Tracking. Incorporating forecasts of obstacle future trajectories can significantly enhance planning performance. Currently, obstacle tracking can be divided into learning-based, physics-based, and hybrid methods. Learning-based methods require large datasets and substantial computational resources for training [24], [25]. Physics-based methods (e.g., Kalman filter [4]) capitalize on prior knowledge for high computational efficiency, while relying on predefined kinematic models that introduce inevitable bias and limit the ability to handle complex motions, especially when the state transition model is partially observed. Lastly, hybrid methods combine strengths of both categories, resulting in efficient and adaptable physics-informed learning solutions. For example, the recent KalmanNet [5] mitigates the drawbacks of Kalman filters by learning the Kalman gain from real data, so as to maintain both high inference accuracy and lightweight model size. This work extends physics-informed learning to Doppler LiDAR, which has not been studied yet.

Motion Planning. Many modern motion planning systems (e.g., robot, autonomous vehicle) are based on MPC, which generates optimal control outputs in response to environmental inputs within a receding horizon window [26], [27]. By incorporating obstacle tracking, MPC can construct time-varying constraints and handle dynamic environments [8]. In general, the MPC performance depends on the problem modeling. To find the best setting, auto-tuning MPC [28], [29] uses closed-loop feedback to optimize controller parameters. However, it typically involves time-consuming data collections and requires actual collision events to trigger parameter learning. In contrast, our proposed DT-MPC achieves run-time MPC tuning by leveraging Doppler-inferred collisions, thereby boosting the robustness for handling rapid-motion obstacles.

III. PROBLEM FORMULATION

We consider an MPC motion planner operating among N dynamic obstacles $\mathcal{N} = \{1, \dots, N\}$. At time t , the MPC horizon is represented by a finite sequence of H discretized future steps $\mathcal{H}_t \triangleq \{t, \dots, t+H-1\}$, where Δt is the time length between two states. Let $\mathbf{s}_h = (x_h, y_h, \theta_h)$ be the robot state, where (x_h, y_h) and θ_h are position and orientation at the bottom center of the corresponding bounding box $\mathbb{G}_h(\mathbf{s}_h)$, respectively. Let $\mathbf{w}_h = (v_h, \psi_h)$ be the robot action, where v_h and ψ_h are linear and angular velocity, respectively. By iterating over \mathcal{H}_t , the MPC system finds an optimal state sequence $\mathcal{S}_t = \{\mathbf{s}_{t+1}, \mathbf{s}_{t+2}, \dots, \mathbf{s}_{t+H}\}$ via action sequence $\mathcal{W}_t = \{\mathbf{w}_t, \mathbf{w}_{t+1}, \dots, \mathbf{w}_{t+H-1}\}$, where $\{\mathcal{W}_t, \mathcal{U}_t\} \in \mathcal{F}_t$, with \mathcal{F}_t being the kinematic constraint detailed in Section IV. The problem is thus formulated as

$$P_t : \min_{\{\mathcal{W}_t, \mathcal{U}_t\} \in \mathcal{F}_t} C_t(\mathcal{S}_t) \quad (1a)$$

$$\text{s.t.} \quad \text{dist}(\mathbb{G}_{h+1}, \mathbb{O}_{h+1}^n) \geq d_{\text{safe}}, \forall h \in \mathcal{H}_t, n \in \mathcal{N}, \quad (1b)$$

where $C_t(\mathcal{S}_t)$ is the utility function, d_{safe} is the safety distance, and $(\mathbb{G}_{h+1}, \mathbb{O}_{h+1}^n)$ are bounding boxes of ego-robot and the n -th obstacle, respectively. The minimum distance function between two bounding boxes is defined as:

$$\text{dist}(\mathbb{P}, \mathbb{Q}) = \min_{\mathbf{p}, \mathbf{q}} \|\mathbf{p} - \mathbf{q}\|_2, \text{ s.t. } \mathbf{p} \in \mathbb{P}, \mathbf{q} \in \mathbb{Q}. \quad (2)$$

Considering a reference path tracking task with target waypoints $\{\mathbf{s}_{h+1}^* | h \in \mathcal{H}_t\}$, we formulate $C_t(\mathcal{S}_t) = \sum_{h \in \mathcal{H}_t} \|\mathbf{s}_{h+1} - \mathbf{s}_{h+1}^*\|_2^2$ [12].

Problem P_t is nontrivial since estimating \mathbb{O}_{h+1}^n results in inevitably biased $\hat{\mathbb{O}}_{h+1|t}^n$, which can significantly mismatch the actual \mathbb{O}_{h+1}^n if obstacle n has rapid motions. This error would further propagate to motion planning since $\text{dist}(\mathbb{G}_{h+1}, \hat{\mathbb{O}}_{h+1|t}^n) \neq \text{dist}(\mathbb{G}_{h+1}, \mathbb{O}_{h+1}^n)$.

IV. DOPPLER PLANNING NETWORK

To solve P_t among rapid-motion obstacles, we propose D-KalmanNet for reducing the uncertainty of $\hat{\mathbb{O}}_{h+1|t}^n$ and DT-MPC for robustifying the solution by real-time tuning d_{safe} . We then integrate them into a unified solution, DPNet, whose overall architecture is shown in Fig. 2. It takes the Doppler LiDAR point cloud \mathcal{P}_t as input and outputs the actions \mathcal{W}_t .

A. Doppler KalmanNet for Tracking

The ego robot uses a Doppler LiDAR to scan the surrounding environment and obtains $\mathcal{P}_t = \{\mathbf{c}_t^i, \|\boldsymbol{\mu}_t^i\|_2\}_{i=1}^I$, where I is the number of points in the frame, $\mathbf{c}_t^i \in \mathbb{R}^3$ and $\|\boldsymbol{\mu}_t^i\|_2 \in \mathbb{R}$ are the spatial coordinate and the scalar Doppler velocity of the i -th point, respectively. Accordingly, we define the Doppler-augmented state \mathbf{x}_t^n as

$$\mathbf{x}_t^n = [x_t^n, \cos \theta_t^n v_t^n, \cos \theta_t^n a_t^n, y_t^n, \sin \theta_t^n v_t^n, \sin \theta_t^n a_t^n]^\top, \quad (3)$$

where (x_t^n, y_t^n) , θ_t^n , v_t^n and a_t^n represent the position, orientation, linear velocity and acceleration at the center, respectively. Each \mathbf{x}_t^n can be used to generate a \mathbb{O}_t^n . Hence, we only need to estimate a sequence of $\{\hat{\mathbf{x}}_{t+1|t}^n, \hat{\mathbf{x}}_{t+2|t}^n, \dots, \hat{\mathbf{x}}_{t+H|t}^n\}$ from \mathcal{P}_t . We can fuse \mathcal{P}_t with a state transition model to achieve

Algorithm 1 D-KalmanNet

Input: $\{\mathbf{y}_0^n, \mathbf{y}_1^n, \dots\}_{n=1}^N$
Output: $\{\hat{\mathbb{O}}_0^n, \hat{\mathbb{O}}_1^n, \dots\}_{n=1}^N$

- 1: Initialize $t = 0$
- 2: **while** *True* **do**
- 3: **for** $n \in \mathcal{N}$ **do**
- 4: Group Doppler LiDAR point cloud as \mathcal{P}_t^n
- 5: Obtain \mathbf{y}_t^n from Doppler Velocity Rectification
- 6: **if** $t = 0$ **then**
- 7: $\mathbf{x}_0^n \leftarrow \mathbf{y}_0^n, \hat{\mathbf{x}}_{1|0}^n \leftarrow \mathbf{T} \cdot \mathbf{x}_0^n, \hat{\mathbf{y}}_{1|0}^n \leftarrow \mathbf{U} \cdot \hat{\mathbf{x}}_{1|0}^n$
- 8: **else**
- 9: $\mathcal{K}_t^n \leftarrow \text{RNN}(\mathbf{x}_{t-1}^n, \hat{\mathbf{x}}_{t|t-1}^n, \hat{\mathbf{y}}_{t|t-1}^n, \mathbf{y}_t^n)$
- 10: $\mathbf{x}_t^n \leftarrow \hat{\mathbf{x}}_{t|t-1}^n + \mathcal{K}_t^n \cdot (\mathbf{y}_t^n - \hat{\mathbf{y}}_{t|t-1}^n)$
- 11: $\hat{\mathbf{x}}_{h+1|t}^n \leftarrow \mathbf{T}^{h-t+1} \cdot \mathbf{x}_t^n, \forall h \in \mathcal{H}_t$
- 12: $\hat{\mathbf{y}}_{t+1|t}^n \leftarrow \mathbf{U} \cdot \hat{\mathbf{x}}_{t+1|t}^n$
- 13: **end if**
- 14: **end for**
- 15: Generate $\hat{\mathbb{O}}_t^n$ from $\{\hat{\mathbf{x}}_{t+1|t}^n, \hat{\mathbf{x}}_{t+2|t}^n, \dots, \hat{\mathbf{x}}_{t+H|t}^n\}$
- 16: **return** $\hat{\mathbb{O}}_t^n$ and $t \leftarrow t + 1$
- 17: **end while**

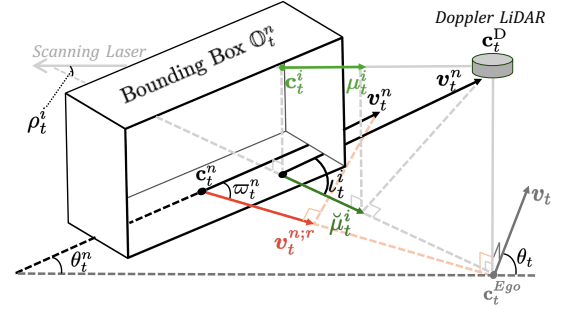


Fig. 3: Doppler velocity rectification.

this goal, but two challenges exist. First, according to Doppler LiDAR manufacturers [14], real-world velocity measurements typically involve noises with standard deviation of 0.1 m/s. Second, built upon past trajectories, the transition model may mismatch the actual obstacle motions in the future [5]. Our D-KalmanNet can simultaneously tackle both challenges.

1) *Doppler Velocity Rectification:* We propose Doppler velocity rectification shown in Fig. 3 to address the first challenge. Our observation is that any measurement point on a common obstacle with a rigid-body motion would share the same linear velocity. As such, it is possible to aggregate velocities across dense points for mitigating the Doppler LiDAR noise. Since different lasers hit different points on obstacle surfaces and reflect different radial velocities, we first unify the measurements to the same vector direction. Specifically, let $\mathbf{c}_t^n, \mathbf{c}_t^{\text{ego}} \in \mathbb{R}^3$ represent positions of obstacle bottom center and ego robot bottom center, respectively. The Doppler LiDAR mounted at $\mathbf{c}_t^{\text{D}} \in \mathbb{R}^3$ emits its i -th scanning laser with a scanning elevation angle ρ_t^i , hitting and reflecting from point \mathbf{c}_t^i . The Doppler velocity projection $\check{\boldsymbol{\mu}}_t^i$ on the 2D plane is derived as:

$$\check{\boldsymbol{\mu}}_t^i = \|\boldsymbol{\mu}_t^i\|_2 \cos \rho_t^i \frac{(\mathbf{I} - \mathbf{e}\mathbf{e}^\top)(\mathbf{c}_t^{\text{D}} - \mathbf{c}_t^i)}{\|(\mathbf{I} - \mathbf{e}\mathbf{e}^\top)(\mathbf{c}_t^{\text{D}} - \mathbf{c}_t^i)\|_2}, \quad (4)$$

where $\mathbf{e} = [0 \ 0 \ 1]^\top$ and $\mathbf{I} \in \mathbb{R}^{3 \times 3}$ is an identity matrix.

Algorithm 2 Doppler Collision Check and Tuning

```

1: Initialize  $\mathcal{S}_{t-1} = \emptyset$ 
2: while True do
3:    $\varrho_n \leftarrow \infty$  for  $n \in \mathcal{N}$ 
4:    $\kappa \leftarrow \kappa^{\text{init}}$ 
5:   Obtain  $\hat{\mathcal{O}}_t^n$  from the D-KalmanNet
6:   for  $h \in \mathcal{H}_{t-1}^-$  do
7:     for  $n \in \mathcal{N}$  do
8:       if  $\varrho_n = \infty$  and  $\text{dist}(\mathbb{G}_{h+1}^\circ, \hat{\mathcal{O}}_{h+1|t}^n) \leq d_0$  then
9:          $\varrho_n \leftarrow \kappa$ 
10:      end if
11:    end for
12:    Update  $\kappa \leftarrow \kappa + \Delta\kappa$ 
13:  end for
14:   $t \leftarrow t + 1$ 
15: end while

```

With the above vector projection, we conduct Doppler LiDAR measurement grouping which clusters points within the obstacle's bounding box as

$$\mathcal{P}_t^n = \{\{\mathbf{c}_t^i, \|\boldsymbol{\mu}_t^i\|_2\} | \mathbf{c}_t^i \sqsubseteq \mathbb{O}_t^n\} = \{p_t^{i,n}\}_{i,n=1}^{I_n}, \quad (5)$$

where $p_t^{i,n}$ is the i_n -th point of group \mathcal{P}_t^n , \sqsubseteq is an operator that indicates being within the spatial boundary. Lastly, denote ϖ_t^n as the angle between \mathbf{v}_t^n and the center radial velocity $\mathbf{v}_t^{n;r}$ and ι_t^i as the angle between \mathbf{v}_t^n and the Doppler velocity projection $\check{\boldsymbol{\mu}}_t^i$. We have rigid motion consistency $\mathbf{v}_t^{n;r} \cos \iota_t^i = \check{\boldsymbol{\mu}}_t^i \cos \varpi_t^n$. Therefore, the fused linear velocity \mathbf{v}_t^n is given by

$$\mathbf{v}_t^n = \frac{1}{|I_n|} \sum_{i_n=1}^{I_n} \frac{1}{\cos \iota_t^{i_n}} \check{\boldsymbol{\mu}}_t^{i_n}. \quad (6)$$

2) *Kalman Gain Learning*: We propose Kalman gain learning to address the second challenge. We set up a partially observable GSS model for the dynamics, whose state transition model is \mathbf{T} (assuming a constant acceleration) and state observation model is \mathbf{U} (involving both position and velocity). Then we have the following state transition

$$\hat{\mathbf{x}}_{h+1|h}^n = \mathbf{T}\mathbf{x}_h^n, \quad \hat{\mathbf{y}}_{h+1|h}^n = \mathbf{U}\hat{\mathbf{x}}_{h+1|h}^n, \quad (7)$$

where $\hat{\mathbf{x}}_{h+1|h}^n$ is the priori state prediction and $\hat{\mathbf{y}}_{h+1|h}^n$ is the estimated state observation using forward propagation. After Δt , LiDAR scan \mathcal{P}_{h+1} arrives, providing the actual \mathbf{y}_{h+1}^n by equations (3) and (6). We then update the posteriori state prediction by

$$\mathbf{x}_{h+1}^n = \hat{\mathbf{x}}_{h+1|h}^n + \mathcal{K}_{h+1}^n \cdot (\mathbf{y}_{h+1}^n - \hat{\mathbf{y}}_{h+1|h}^n), \quad (8)$$

where \mathcal{K}_{h+1}^n is the learned Kalman gain:

$$\mathcal{K}_{h+1}^n = \text{RNN}(\mathbf{x}_h^n, \hat{\mathbf{x}}_{h+1|h}^n, \hat{\mathbf{y}}_{h+1|h}^n, \mathbf{y}_{h+1}^n). \quad (9)$$

Particularly, we adopt an RNN [5] to learn a robust and adaptive \mathcal{K}_{h+1}^n for posteriori update, thereby alleviating the noises originated from either mismatched \mathbf{T} or inaccurate $\mathbf{y}_{h+1|h}^n$. The entire procedure is summarized in Algorithm 1, where $\hat{\mathcal{O}}_t^n = \{\hat{\mathcal{O}}_{h+1|t}^n(\hat{\mathbf{x}}_{h+1|t}^n) | \forall h \in \mathcal{H}_t\}$ represents the set of bounding box predictions over the planning horizon.

B. Doppler-Tuned MPC for Planning

With the Doppler-learned $\{\hat{\mathcal{O}}_0^n, \hat{\mathcal{O}}_1^n, \dots\}_{n=1}^N$ from D-KalmanNet (Algorithm 1), we propose DT-MPC which enables real-time controller tuning by leveraging Doppler-inferred collision check. According to [28], [29], the core of controller tuning is transforming the fixed value d_{safe} in \mathbf{P}_t into a learnable parameter vector $\phi = [\phi_{t+1,1}, \dots, \phi_{t+H,N}]^T$. As such, \mathbf{P}_t becomes a parameter optimization problem

$$\mathbf{Q}_t : \min_{\{\mathcal{W}_t, \mathcal{S}_t\} \in \mathcal{F}_t, \phi \in \Phi} C_t(\mathcal{S}_t) + \gamma \mathcal{L}(\phi, \{\hat{\mathcal{O}}_t^n\}), \quad (10a)$$

where \mathcal{L} is the closed-loop collision cost function, γ is the collision penalty coefficient and Φ defines the upper and lower bounds of ϕ . One example of \mathcal{L} is the quadratic loss of the collision penalty [27], where

$$\mathcal{L}(\phi, \{\hat{\mathcal{O}}_t^n\}) = \sum_{h \in \mathcal{H}_t} \sum_{n \in \mathcal{N}} \left\| \min \left(\text{dist}(\mathbb{G}_{h+1}, \hat{\mathcal{O}}_{h+1|t}^n) - \phi_{h+1,n}, 0 \right) \right\|^2. \quad (11)$$

1) *Doppler-Inferred Collision Check*: In conventional auto-tuning MPC [27], \mathbf{Q}_t is solved by differentiable optimization with gradient update to yield a larger ϕ when the robot collides with any obstacle, yet can be inefficient if collision events are sparse. In contrast, in our system, we have highly-accurate (as demonstrated in Section V-B) prediction $\hat{\mathcal{O}}_{h+1|t}^n$ provided by D-KalmanNet. Moreover, for an MPC system, although solving \mathbf{Q}_t provides the complete solution sequence of \mathcal{W}_t and \mathcal{S}_t along \mathcal{H}_t , only the first action \mathbf{w}_t is executed and ends up with state \mathbf{s}_{t+1} , resulting in a sequence of non-executed actions $\mathcal{W}_t^\circ = \{\mathbf{w}_h\}_{h=t+1}^{t+H-1}$ and a sequence of potential states $\mathcal{S}_t^\circ = \{\mathbf{s}_h\}_{h=t+2}^{t+H}$. Hence, by leveraging \mathcal{W}_t° and \mathcal{S}_t° as a prediction of ego-trajectory, and obstacle-trajectory prediction $\hat{\mathcal{O}}_{h+1|t}^n$ from D-KalmanNet, a Doppler-inferred collision check can be formulated to enable run-time MPC tuning. Specifically, let $\mathcal{H}_{t-1}^- = \mathcal{H}_{t-1} \setminus \{t-1\}$ denote the truncated historical horizon at time t . The bounding box sequence of historical potential states \mathcal{S}_{t-1}° is denoted as

$$\mathcal{G}_{t-1}^\circ = \{\mathcal{G}_{h+1}^\circ(\mathbf{s}_{h+1}) | \mathbf{s}_{h+1} \in \mathcal{S}_{t-1}^\circ, \forall h \in \mathcal{H}_{t-1}^-\}, \quad (12)$$

Since \mathcal{H}_{t-1}^- ends at $t+H-2$, the last element of $\hat{\mathcal{O}}_t^n$ is also truncated to match the length. The criteria of potential collision along the truncated historical horizon is

$$\text{dist}(\mathbb{G}_{h+1}^\circ, \hat{\mathcal{O}}_{h+1|t}^n) \leq d_0, \forall h \in \mathcal{H}_{t-1}^-, n \in \mathcal{N}, \quad (13)$$

where d_0 is the collision threshold.

2) *Run-Time Auto-Tuning*: Now, if Doppler-inferred collision (13) exists for any obstacle, the MPC parameters ϕ for current planning round can be auto-tuned to cope with potential future risks. Specifically, $\phi_{h,n}$ is decomposed into a constant component and an adaptive component as $\phi_{h,n} = d_1 + \tau(n, h)d_2$, where d_1 is the compulsory minimum distance and $\tau(n, h)d_2$ is the Doppler adaptive distance. This converts tuning $\phi_{h,n}$ to tuning the factor $\tau(n, h)$, and allows us to adopt a simple yet effective parameter update method to surrogate for the gradient $\partial \mathcal{L} / \partial \tau(n, h)$. Denoting $\tau(n, h) = \tau_1(n)\tau_2(h)$, where $\tau_1(n) \in (0, 1)$ is the spatial factor and $\tau_2(h) \in (0, 1)$ is the temporal factor, the update is performed as follows:

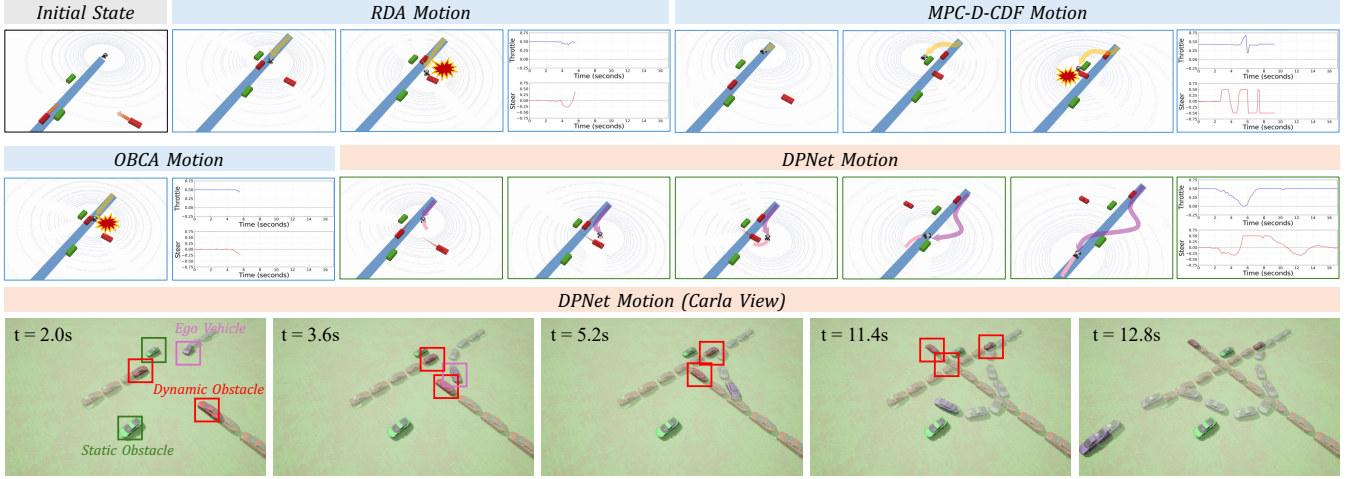


Fig. 4: Qualitative analysis of robot motions (in ROS-Rviz and Carla [13] views) and corresponding control commands. Static obstacles are marked as green boxes, while dynamic ones are red boxes with arrows indicating their moving directions. The blue line is the path connecting start and goal points. The dots in front of dynamic obstacles represent motion predictions.

First, the spatial factor $\tau_1(n)$ measures the imminence of the Doppler-inferred collision by

$$\tau_1(n) = \max(1 - \alpha(\varrho_n - \kappa^{\text{init}}), \tau_{1;\min}), \quad (14)$$

where $\tau_{1;\min}$ is the lower bound, $\alpha \in (0, 1)$ is the decay rate, and ϱ_n is the collision priority assigned chronologically. A larger α leads to a higher focus on imminent collisions. Algorithm 2 details how ϱ_n is assigned using the accumulator κ , which starts with κ^{init} and increments by $\Delta\kappa$ along the horizon. Second, the temporal factor $\tau_2(h)$ accounts for the inherently increasing uncertainty of farther predictions:

$$\tau_2(h) = \max(1 - \beta(h - t), \tau_{2;\min}), \quad (15)$$

where $\tau_{2;\min}$ is the lower bound and $\beta \in (0, 1)$ is the horizon decay rate. A larger β imposes stricter constraints on nearby predictions while relaxing constraints for distant ones.

3) *Solution by ADMM*: With the Doppler-tuned $\hat{\phi}$ from DT-MPC (Algorithm 2), Q_t is explicitly written as

$$R_t : \min_{\mathcal{W}_t, S_t} C_t(S_t) + \gamma \mathcal{L}(\hat{\phi}, \{\hat{O}_t^n\}), \quad (16a)$$

$$\text{s.t.} \quad \mathbf{s}_{h+1} = \mathbf{s}_h + f(\mathbf{s}_h, \mathbf{w}_h) \Delta t, \quad \forall h, \quad (16b)$$

$$\mathbf{w}_{\min} \preceq \mathbf{w}_h \preceq \mathbf{w}_{\max}, \quad \forall h, \quad (16c)$$

where (16b) represents the state evolution ($f(\cdot)$ defines vehicle dynamics) and (16c) represents the physical constraint ($\mathbf{w}_{\min}, \mathbf{w}_{\max}$ are control limits), i.e., the kinematic set \mathcal{F}_t explicitly becomes $\mathcal{F}_t = \{(16b), (16c)\}$ [12].

The only nonconvex part in R_t is $\mathcal{L}(\hat{\phi}, \{\hat{O}_t^n\})$. To tackle this function, we can equivalently transform \mathcal{L} into a biconvex form using Lagrange duality [10], [27], and then solve the resultant biconvex version by ADMM. This ADMM will converge to a stationary point of R_t .

V. EXPERIMENTS

We implement DPNet in ROS Noetic on Linux system. We compare DPNet with state-of-the-art methods and provide both qualitative and quantitative results in heterogeneous

scenarios. The experiments are conducted using Carla simulator with Doppler LiDAR integration [23]. Moreover, we evaluate the proposed D-KalmanNet against existing obstacle tracking methods to assess the robustness in highly-dynamic environments and on resource-constrained platforms. The D-KalmanNet is trained for 2000 epochs using Doppler LiDAR measurements and ground truth vehicle trajectories, using the real-world dataset AevaScenes [14].

A. End-to-End Evaluation in Carla

We compare the following methods¹ for end-to-end evaluations in Carla-ROS simulation: (1) **DPNet**: our proposed method; (2) **MPC-D-CBF** [11]: an MPC-based planner that predicts obstacle motion using LiDAR and Kalman filter, constructing D-CBFs online for navigation among moving obstacles; (3) **RDA** [10]: an MPC-based planner that uses parallelizable dual ADMM to accelerate agile collision avoidance; (4) **OBCA** [12]: an MPC-based planner with optimization-based collision avoidance for convex obstacles; (5) **DPNet (Ablation)**: our proposed method where DT-MPC is disabled. All methods are set up with $H = 15$ and $\Delta t = 0.12s$. Ego robot and obstacles are modeled as car-like wheel robots.

Qualitative Analysis. As shown in Fig. 4, this scenario consists of two static obstacles and two rapid-motion obstacles (at 5 m/s), one with vertical direction and the other with lateral direction. These obstacles *will not avoid the ego robot*. The ego robot needs to traverse the area while avoiding collisions with any obstacle. It can be seen that our proposed DPNet succeeds to pass through the area with agile motions. Particularly, at $t = 2s$, if velocity information is ignored, directly passing between the two dynamic objects appears to be the optimal choice. This is case of RDA, which crashes into the lateral moving obstacle at $t = 5.6s$. The is because at $t = 4s$,

¹Reinforcement learning baselines are not included, since they suffer from a lack of safety assurance in highly-dynamic scenarios. For example, we have tested twin delayed deep deterministic policy gradient algorithm (TD3) in IR-SIM [10], with 15 obstacles randomly moving at 2 m/s in a 40m×40m square. The success rate of TD3 is only 70/100.

Metric	Method				
	OBCA [12]	RDA [10]	MPC-D-CBF [11]	DPNet (Ablation)	DPNet
1D-1S clutter level					
AvgAcc ↓	1.189	1.196	1.186	1.172	1.170
MaxAcc ↓	7.142	8.594	7.532	5.697	6.698
AvgJerk ↓	5.458	5.849	5.544	6.081	5.078
ItTime ↓	0.124	0.081	0.107	0.083	0.083
PassTime ↓	10.901	10.418	11.325	9.508	9.506
PassRate ↑	84.0	93.0	99.0	100.0	100.0
2D-2S clutter level					
AvgAcc ↓	1.534	1.705	1.655	1.548	1.479
MaxAcc ↓	7.744	8.689	8.036	7.201	7.019
AvgJerk ↓	6.629	7.001	6.827	6.393	6.219
ItTime ↓	0.150	0.096	0.130	0.105	0.108
PassTime ↓	11.553	11.125	12.049	10.600	10.461
PassRate ↑	71.0	80.0	93.0	97.0	98.0
4D-4S clutter level					
AvgAcc ↓	1.581	1.644	1.709	1.322	1.310
MaxAcc ↓	7.998	8.366	8.471	7.560	7.424
AvgJerk ↓	6.330	6.559	6.937	6.346	6.313
ItTime ↓	0.163	0.117	0.164	0.126	0.131
PassTime ↓	13.544	13.287	14.442	12.861	11.792
PassRate ↑	46.0	59.0	72.0	77.0	82.0
6D-6S clutter level					
AvgAcc ↓	1.327	1.478	1.310	1.294	1.288
MaxAcc ↓	8.421	8.015	8.138	7.559	7.458
AvgJerk ↓	5.758	6.032	5.999	5.743	5.679
ItTime ↓	0.185	0.141	0.189	0.140	0.148
PassTime ↓	16.766	15.139	16.509	14.320	12.887
PassRate ↑	10.0	24.0	45.0	52.0	61.0

TABLE I: Performance comparison at different clutter levels. Purple denotes the **best** performance.

the ego-robot is completely surrounded by four obstacles, and it was too late to steer by then. In contrast, *with accurate velocity understanding, our DPNet can look ahead into the future, “imaging” that directly passing through is risky, and thus early-executes the left-turn at $t = 2s$* . As such, at $t = 3.6s$ and $t = 5.2s$, the ego-robot bypasses from behind the laterally moving obstacle. This demonstrates the power of Doppler model-based learning in handling highly-dynamic environments. In terms of other methods, the OBCA planner crashes into the vertical moving obstacle due to its delayed motions caused by low computation frequency. The MPC-D-CBF planner makes over-conservative decision upon handling the vertical moving obstacle due to its inaccurate velocity understandings, resulting in a crash finally.

Quantitative Analysis. As shown in Fig. 5, we set up 4 scenes with different environmental clutter levels to evaluate detailed performances. A higher clutter level means more dynamic and static obstacles, with dynamic obstacles assigned fixed directions and a velocity of 5 m/s. The following six metrics are used: (a) **AvgAcc** (m/s^2): the average acceleration during the execution; (b) **MaxAcc** (m/s^2): the maximum acceleration during the execution; (c) **AvgJerk** (m/s^3): the average jerk during the execution; (d) **ItTime** (s): the average iteration time of the solver during the execution; (e) **PassTime** (s): the average time duration to traverse the area; (f) **PassRate** (%): the rate of successfully traversing the area without collisions. Experiments are executed 100 times for each setting.

Results are reported in Table I. As clutter level increases,

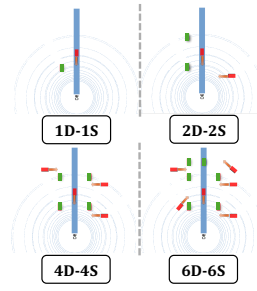


Fig. 5: Clutter levels. D (S) refers to dynamic (static) obstacles.

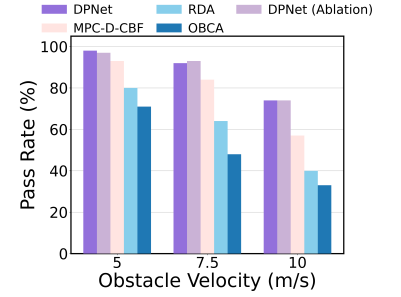


Fig. 6: Pass rate comparison at different obstacle velocities in 2D-2S clutter level.

DPNet consistently outperforms all benchmark methods, in terms of both motion smoothness and time efficiency. Furthermore, ablation studies demonstrate that DT-MPC effectively improves the navigation performance compared to its non-DT counterpart, at the cost of a slight increase in execution time. This confirms the enhanced adaptability of DT-MPC to properly tune safety distances online, especially in high clutter levels. To further assess DPNet’s agility in highly-dynamic environments, we compare pass rate under varying obstacle velocity conditions. Experiments are conducted in the 2D-2S scene with three different obstacle velocities: 5 m/s, 7.5 m/s, and 10 m/s. As illustrated in Fig. 6, results demonstrate that DPNet maintains a high pass rate across all velocities, highlighting its robustness in the presence of fast-moving obstacles.

B. Evaluation on Real-World Datasets

To evaluate D-KalmanNet’s robustness to real-world sensor noises, we conduct experiments on the AevaScene [14] dataset, which contains on-road Doppler LiDAR data and ground truth annotations of vehicle trajectories in both *Highway* and *City* scenarios. Following methods are compared: (1) **D-KNet**: our proposed tracking method; (2) **KNet** [5]: the KalmanNet, a physics-informed deep learning method; (3) **KF** [11]: the Kalman filter, a widely-used conventional tracking method; (4) **D-KF** [18]: the conventional Kalman filter aided by Doppler LiDAR.

To quantify tracking accuracy, we use the normalized mean squared error (NMSE) in decibels (dB) following [5]. Specifically, for each vehicle, and at every feasible time step t , we first evaluate the horizon-averaged NMSE over \mathcal{H}_t :

$$NMSE_t = \frac{1}{H} \sum_{h \in \mathcal{H}_t} \frac{(\hat{x}_{h+1|t} - x_{h+1})^2 + (\hat{y}_{h+1|t} - y_{h+1})^2}{x_{h+1}^2 + y_{h+1}^2},$$

where $(\hat{x}_{h+1|t}, \hat{y}_{h+1|t})$ and (x_{h+1}, y_{h+1}) denote the predicted and ground-truth obstacle positions, respectively. We then convert to the logarithmic scale via $10 \log_{10}(\cdot)$ to obtain a per-step dB-NMSE score. These scores are averaged over vehicle trajectory length to yield a single dB-NMSE value per vehicle, and finally aggregated across all vehicles as **mean \pm std**.

Qualitative Analysis. Fig. 7 demonstrates a visualized result of tracking one rapidly approaching vehicle (at about 25 m/s) on the *Highway* scenario. Among the evaluated methods, D-KNet demonstrates superior performance by effectively

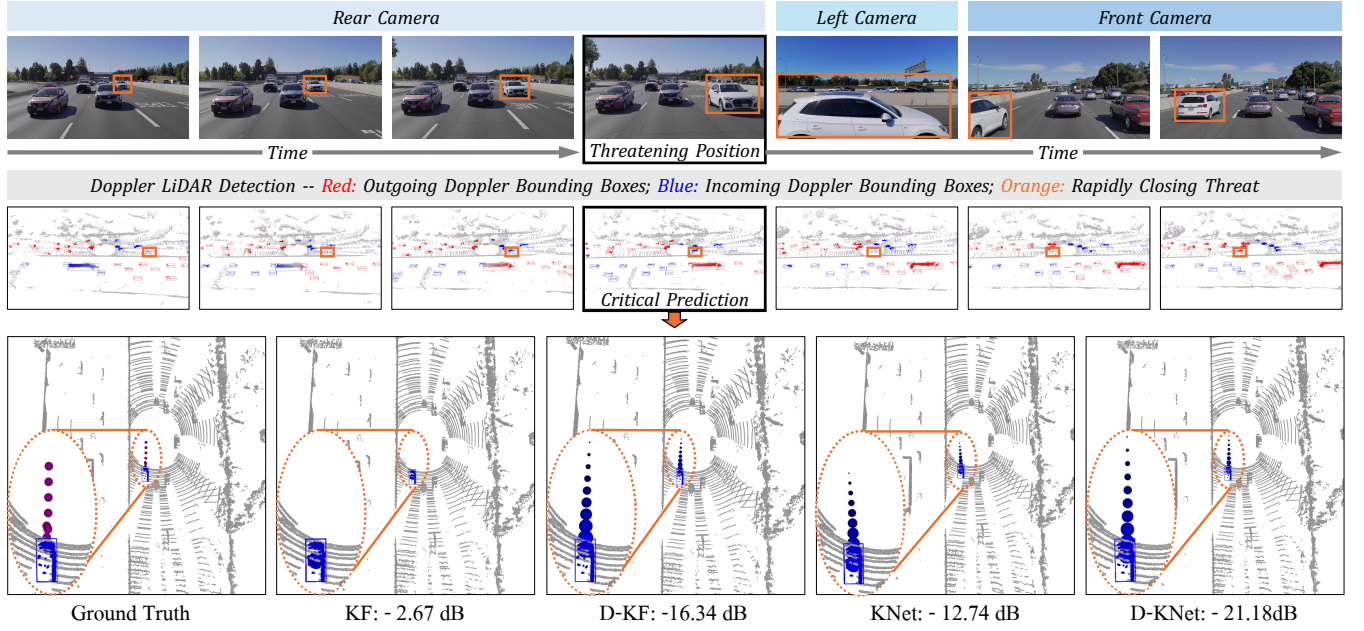


Fig. 7: Visualization of critical predictions for a rapidly approaching vehicle (at about 25 m/s, highlighted in orange) in *Highway* scenario of AevaScene [14]. The upper half shows Doppler LiDAR’s environmental dynamics detection (outgoing/incoming bounding boxes marked in red/blue). The lower half provides detailed comparison of trajectory predictions for the threat.

\mathcal{H}_t	Method	Tracking Frequency		
		10 Hz	5 Hz	2 Hz
5	-	<i>Highway scenario</i>		
	KF [11]	-22.66 \pm 6.41	-16.62 \pm 5.24	-7.18 \pm 3.84
	KNet [5]	-23.38 \pm 7.82	-17.79 \pm 7.77	-12.56 \pm 7.16
	D-KF [18]	-27.15 \pm 6.39	-21.66 \pm 4.77	-14.09 \pm 3.60
	D-KNet	-35.80 \pm 8.62	-29.11 \pm 7.17	-20.22 \pm 2.45
	-	<i>City scenario</i>		
10	KF [11]	-27.15 \pm 6.35	-20.48 \pm 4.79	-9.15 \pm 6.64
	KNet [5]	-29.26 \pm 5.47	-23.66 \pm 5.98	-17.38 \pm 7.36
	D-KF [18]	-32.74 \pm 6.18	-27.60 \pm 5.11	-19.20 \pm 5.03
	D-KNet	-45.00 \pm 7.35	-37.67 \pm 6.11	-29.63 \pm 6.76
	-	<i>Highway scenario</i>		
	KF [11]	-18.50 \pm 6.53	-11.49 \pm 5.92	1.88 \pm 6.47
10	KNet [5]	-17.50 \pm 7.49	-11.83 \pm 7.64	-6.32 \pm 6.73
	D-KF [18]	-23.68 \pm 6.44	-17.36 \pm 4.65	-6.61 \pm 4.92
	D-KNet	-26.28 \pm 8.33	-18.88 \pm 6.60	-8.56 \pm 4.66
	-	<i>City scenario</i>		
	KF [11]	-22.55 \pm 6.46	-14.14 \pm 5.27	8.05 \pm 0.30
	KNet [5]	-23.19 \pm 5.54	-17.34 \pm 6.12	-9.81 \pm 8.92
10	D-KF [18]	-29.67 \pm 6.90	-22.97 \pm 5.59	-10.59 \pm 7.26
	D-KNet	-34.30 \pm 7.65	-25.96 \pm 6.82	-16.41 \pm 9.47

TABLE II: NMSE (dB) of motion prediction: **mean** \pm **std** across tracking frequencies and scenarios on the AevaScenes [14] dataset. **Purple** denotes the **best** mean.

leveraging Doppler cues to enable accurate, real-time tracking of rapid objects, achieving the lowest tracking error of -21.18 dB. In contrast, KF and KNet struggle to handle the approaching vehicle with abrupt accelerations. This comparison highlights the importance of integrating model-based learning and Doppler LiDAR measurements for more robust tracking under highly-dynamic conditions.

Quantitative Analysis. Table II reports the results across tracking frequencies (2-10 Hz), prediction horizons (\mathcal{H}_t =

Obstacle Number	1	2	3	4	5	8	10
Execution Time (s)	0.008	0.016	0.025	0.032	0.037	0.050	0.070
Frequency (Hz)	126.57	62.08	39.93	31.53	27.10	19.87	14.36
CPU Usage (%)	5.0	8.0	27.0	38.0	40.0	41.0	42.0

TABLE III: D-KNet’s hardware efficiency across tracked obstacle numbers on NVIDIA Jetson Orin NX 16 GB.

5, 10), and driving scenarios (*Highway*, *City*). Across all settings, D-KNet consistently achieves the lowest NMSE and significantly outperforms all baselines. Notably, at $\mathcal{H}_t = 5$, D-KNet attains -45.00 ± 7.35 dB in the *City* scenario at 10 Hz and surpasses the second best D-KF [18] by 12.26 dB. Even at $\mathcal{H}_t = 10$, D-KNet maintains robustness to long-horizon uncertainty, whereas other methods suffer considerable degradation. Tighter standard deviations of D-KNet further confirm its stability across diverse obstacle dynamics. These results demonstrate the superior reliability of D-KNet, especially under real-world constraints such as varying sensor noise, limited processing frequency, and scenario complexity.

C. More Quantitative Results

We also deploy D-KNet on an NVIDIA Jetson Orin NX 16 GB to evaluate its real-time tracking efficiency on a resource-constrained edge platform. It is found that D-KNet consumes only about 107 MB of GPU memory. As seen from Table III, it achieves inference rates of over 100 Hz when tracking a single fast-moving obstacle. Notably, even with 10 simultaneously tracked obstacles, D-KNet is able to sustain about 15 Hz and a low CPU usage of 42.0 %. These results confirm D-KNet’s suitability for lightweight deployment in real-time autonomous systems.

Table IV shows per-step NMSE (dB) over a 10-step horizon. D-KNet consistently outperforms all baselines at every step, with margin widening especially in short steps (e.g., -48.81

Method	Horizon Step									
	1	2	3	4	5	6	7	8	9	10
<i>Highway scenario</i>										
KF [11]	-15.53 ± 8.80	-15.15 ± 9.63	-14.72 ± 8.45	-14.24 ± 8.26	-13.73 ± 8.09	-13.20 ± 7.90	-12.66 ± 7.72	-12.08 ± 7.53	-11.52 ± 7.33	-10.96 ± 7.15
KNet [5]	-30.82 ± 3.80	-24.80 ± 4.05	-21.44 ± 4.28	-18.93 ± 4.50	-16.93 ± 4.70	-15.24 ± 4.87	-13.78 ± 5.03	-12.42 ± 5.19	-11.23 ± 5.34	-10.16 ± 5.50
D-KF [18]	-16.10 ± 10.37	-16.01 ± 9.51	-15.88 ± 9.19	-15.74 ± 8.91	-15.56 ± 8.64	-15.36 ± 8.47	-15.13 ± 8.33	-14.88 ± 8.23	-14.58 ± 8.14	-14.27 ± 8.10
D-KNet	-41.39 ± 3.23	-34.79 ± 3.34	-30.17 ± 3.47	-26.63 ± 3.58	-23.74 ± 3.73	-21.27 ± 3.90	-19.14 ± 4.10	-17.23 ± 4.29	-15.45 ± 4.52	-13.89 ± 4.74
<i>City scenario</i>										
KF [11]	-16.49 ± 7.12	-16.34 ± 6.83	-16.32 ± 6.69	-16.15 ± 6.54	-15.92 ± 6.42	-15.65 ± 6.30	-15.34 ± 6.17	-14.98 ± 6.04	-14.59 ± 5.91	-14.16 ± 5.77
KNet [5]	-38.22 ± 3.05	-32.42 ± 3.10	-28.90 ± 3.16	-26.26 ± 3.42	-24.13 ± 3.57	-22.3 ± 3.72	-20.68 ± 3.88	-19.22 ± 3.96	-17.87 ± 3.95	-16.59 ± 4.06
D-KF [18]	-16.29 ± 8.89	-16.26 ± 8.19	-16.23 ± 7.78	-16.19 ± 7.47	-16.17 ± 7.26	-16.13 ± 7.07	-16.13 ± 6.88	-16.13 ± 6.68	-16.12 ± 6.51	-16.11 ± 6.34
D-KNet	-48.81 ± 3.01	-41.47 ± 3.09	-36.48 ± 3.21	-32.63 ± 3.25	-29.44 ± 3.17	-27.76 ± 3.31	-24.45 ± 3.57	-22.41 ± 3.62	-20.59 ± 3.65	-18.95 ± 3.76

TABLE IV: NMSE (dB) of per-horizon-step motion prediction for $\mathcal{H}_t = 10$: **mean ± std** across scenarios on the AevaScenes [14] dataset. **Purple** denotes the **best** mean.

dB of DKNet and -16.49 dB of KF for step 1 in *City*). The KF and D-KF methods exhibit nearly flat error growth, indicating trivial estimates under transition model mismatch. However, D-KNet and KNet show physically reasonable error accumulation, demonstrating the effectiveness of model-based learning against dynamics uncertainty. Notably, D-KNet maintains tighter standard deviations and significantly lower mean error, verifying that the Doppler LiDAR integration enhances both accuracy and robustness for long-horizon predictions.

VI. CONCLUSION

This paper has introduced DPNet, a Doppler LiDAR model-based learning method for collision avoidance among rapid-motion obstacles. DPNet achieves both high frequency and accuracy in tracking and planning. Compared to benchmark schemes, it reduces the navigation time by 6%–30%, increases the success rate by up to 16%, and reduces the tracking error by over 10 dB. It was demonstrated that DPNet adapts to platforms with limited computational resources. Ablation studies confirmed the indispensability of incorporating Doppler information into controller tuning and motion planning.

REFERENCES

- [1] Z. Han, M. Tian, Z. Gongye, D. Xue, J. Xing, Q. Wang, Y. Gao, J. Wang, C. Xu, and F. Gao, “Hierarchically depicting vehicle trajectory with stability in complex environments,” *Sci. Robot.*, vol. 10, no. 103, p. eads4551, 2025.
- [2] C. Flores, P. Merdrignac, R. de Charette, F. Navas, V. Milanés, and F. Nashashibi, “A cooperative car-following/emergency braking system with prediction-based pedestrian avoidance capabilities,” *IEEE Trans. Intell. Transp. Syst.*, vol. 20, no. 5, pp. 1837–1846, 2018.
- [3] A. Milan, S. H. Rezatofighi, A. Dick, I. Reid, and K. Schindler, “Online multi-target tracking using recurrent neural networks,” in *Proc. AAAI*, vol. 31, no. 1, 2017.
- [4] V. Lefkopoulou, M. Menner, A. Domahidi, and M. N. Zeilinger, “Interaction-aware motion prediction for autonomous driving: A multiple model kalman filtering scheme,” *IEEE Robot. Autom. Lett.*, vol. 6, no. 1, pp. 80–87, 2020.
- [5] G. Revach, N. Shlezinger, X. Ni, A. L. Escoriza, R. J. Van Sloun, and Y. C. Eldar, “Kalmannet: Neural network aided kalman filtering for partially known dynamics,” *IEEE Trans. Signal Process.*, vol. 70, pp. 1532–1547, 2022.
- [6] H. Liao, C. Wang, Z. Li, Y. Li, B. Wang, G. Li, C. Xu *et al.*, “Physics-informed trajectory prediction for autonomous driving under missing observation,” *Available at SSRN*, vol. 4809575, 2024.
- [7] B. Hessel, H. Vhavle, and Y. Chen, “Dicp: Doppler iterative closest point algorithm,” *arXiv preprint arXiv:2201.11944*, 2022.
- [8] Y. Zhang, G. Tian, L. Wen, X. Yao, L. Zhang, Z. Bing, W. He, and A. Knoll, “Online efficient safety-critical control for mobile robots in unknown dynamic multi-obstacle environments,” in *Proc. IROS*. IEEE, 2024, pp. 12 370–12 377.
- [9] R. Zuliani, E. C. Balta, and J. Lygeros, “Closed-loop performance optimization of model predictive control with robustness guarantees,” *arXiv preprint arXiv:2403.04655*, 2024.
- [10] R. Han, S. Wang, S. Wang, Z. Zhang, Q. Zhang, Y. C. Eldar, Q. Hao, and J. Pan, “Rda: An accelerated collision free motion planner for autonomous navigation in cluttered environments,” *IEEE Robot. Autom. Lett.*, vol. 8, no. 3, pp. 1715–1722, 2023.
- [11] Z. Jian, Z. Yan, X. Lei, Z. Lu, B. Lan, X. Wang, and B. Liang, “Dynamic control barrier function-based model predictive control to safety-critical obstacle-avoidance of mobile robot,” in *Proc. ICRA*, 2023, pp. 3679–3685.
- [12] X. Zhang, A. Liniger, and F. Borrelli, “Optimization-based collision avoidance,” *IEEE Trans. Control Syst. Technol.*, vol. 29, no. 3, pp. 972–983, 2020.
- [13] A. Dosovitskiy, G. Ros, F. Codevilla, A. Lopez, and V. Koltun, “Carla: An open urban driving simulator,” in *Proc. CoRL*, 2017, pp. 1–16.
- [14] G. N. Narasimhan, H. Vhavle, K. B. Vishvanatha, and J. Reuther, “Aevascenes: A dataset and benchmark for fmcw lidar perception,” 2025. [Online]. Available: <https://scenes.aeva.com/>
- [15] R. E. Kalman, “A new approach to linear filtering and prediction problems,” 1960.
- [16] Y. Shi, K. Jiang, X. Zhao, K. Qian, C. Xie, T. Wen, M. Yang, and D. Yang, “Pod: Predictive object detection with single-frame fmcw lidar point cloud,” *arXiv preprint arXiv:2504.05649*, 2025.
- [17] Y. Gu, H. Cheng, K. Wang, D. Dou, C. Xu, and H. Kong, “Learning moving-object tracking with fmcw lidar,” in *Proc. IROS*, 2022, pp. 3747–3753.
- [18] X. Peng and J. Shan, “Detection and tracking of pedestrians using doppler lidar,” *Remote Sens.*, vol. 13, no. 15, p. 2952, 2021.
- [19] Y. Wu, D. J. Yoon, K. Burnett, S. Kammel, Y. Chen, H. Vhavle, and T. D. Barfoot, “Picking up speed: Continuous-time lidar-only odometry using doppler velocity measurements,” *IEEE Robot. Autom. Lett.*, vol. 8, no. 1, pp. 264–271, 2022.
- [20] M. Zhao, J. Wang, T. Gao, C. Xu, and H. Kong, “FMCW-LIO: A doppler lidar-inertial odometry,” *IEEE Robot. Autom. Lett.*, vol. 9, no. 6, pp. 5727–5734, 2024.
- [21] D. J. Yoon, K. Burnett, J. Laconte, Y. Chen, H. Vhavle, S. Kammel, J. Reuther, and T. D. Barfoot, “Need for speed: Fast correspondence-free lidar-inertial odometry using doppler velocity,” in *Proc. IROS*, 2023, pp. 5304–5310.
- [22] M. Zhao, J. Wang, T. Gao, C. Xu, and H. Kong, “Free-init: Scan-free, motion-free, and correspondence-free initialization for doppler lidar-inertial systems,” *IEEE Robot. Autom. Lett.*, vol. 9, no. 12, pp. 11 329–11 336, 2024.
- [23] Aeva-Inc., “Carla-Aeva,” 2024, accessed: 2024-07-08.
- [24] J. Zhou, Y. Gao, O. Johansson, B. Olofsson, and E. Frisk, “Robust predictive motion planning by learning obstacle uncertainty,” *IEEE Trans. Control Syst. Technol.*, vol. 33, no. 3, pp. 1006–1020, 2025.
- [25] R. Zhang, C. Yu, J. Chen, C. Fan, and S. Gao, “Learning-based motion planning in dynamic environments using gnns and temporal encoding,” in *Proc. NeurIPS*, vol. 35, 2022, pp. 30 003–30 015.
- [26] Y. Shi and K. Zhang, “Advanced model predictive control framework for autonomous intelligent mechatronic systems: A tutorial overview and perspectives,” *Annu. Rev. Control.*, vol. 52, pp. 170–196, 2021.
- [27] R. Han, S. Wang, S. Wang, Z. Zhang, J. Chen, S. Lin, C. Li, C. Xu, Y. C. Eldar, Q. Hao *et al.*, “Neupan: Direct point robot navigation with end-to-end model-based learning,” *IEEE Trans. Robot.*, vol. 41, pp. 2804–2824, 2025.
- [28] S. Cheng, M. Kim, L. Song, C. Yang, Y. Jin, S. Wang, and N. Hovakimyan, “Diffune: Auto-tuning through auto-differentiation,” *IEEE Trans. Robot.*, vol. 40, pp. 4085–4101, 2024.
- [29] R. Tao, S. Cheng, X. Wang, S. Wang, and N. Hovakimyan, “Diffune-mpc: Closed-loop learning for model predictive control,” *IEEE Robot. Autom. Lett.*, vol. 9, no. 8, pp. 7294–7301, 2024.